

Fermi and eROSITA Bubbles as Persistent Structures of the Milky Way

JIRO SHIMODA¹ AND KATSUAKI ASANO¹

¹*Institute for Cosmic Ray Research, The University of Tokyo, 5-1-5 Kashiwanoha, Kashiwa, Chiba 277-8582, Japan*

(Received today)

Submitted to ApJ

ABSTRACT

The Fermi and eROSITA bubbles, large diffuse structures in our Galaxy, can be the by-products of the steady star formation activity. To simultaneously explain the star formation history of the Milky Way and the metallicity of $\sim Z_{\odot}$ at the Galactic disk, a steady Galactic wind driven by cosmic-rays is required. For tenuous gases with a density of $\lesssim 10^{-3} \text{ cm}^{-3}$, the cosmic-ray heating dominates over radiative cooling, and the gas can maintain the virial temperature of $\sim 0.3 \text{ keV}$ ideal for escape from the Galactic system as the wind. A part of the wind falls back onto the disk like a galactic fountain flow. We model the wind dynamics according to the Galactic evolution scenario and find that the scale height and surface brightness of the X-ray and the hadronic gamma-ray emissions from such fountain flow region can be consistent with the observed properties of the Fermi and eROSITA bubbles. This implies that the bubbles are persistent structures of the Milky Way existing over (at least) the last $\sim 1 \text{ Gyr}$, rather than evanescent structures formed by non-trivial, $\sim 10 \text{ Myr}$ past Galactic Center transient activities.

Keywords: gamma-rays:ISM — X-rays:ISM — (ISM:) cosmic rays — Galaxy: halo — Galaxy: evolution — ISM: jets and outflows

1. INTRODUCTION

The Fermi and eROSITA bubbles (FBs and eRBs) are the largest gamma-ray and X-ray emitting objects in the sky, respectively (Su et al. 2010; Su & Finkbeiner 2012; Ackermann et al. 2014; Predehl et al. 2020). They look like nearly symmetrical pairs of bubbles rising above and below the center of our Galaxy. The FBs extend about 50° , and their emission mechanism is under debate, whether the leptonic scenario (inverse Compton scattering by relativistic electrons; Mertsch & Sarkar 2011; Mertsch & Petrosian 2019; Cheng et al. 2011, 2014, 2015a; Sasaki et al. 2015; Yang & Ruszkowski 2017) or the hadronic scenario (decay of π^0 particles produced by collisions between relativistic protons and target nuclei in thermal gas; Crocker & Aharonian 2011; Crocker et al. 2015; Fujita et al. 2013; Cheng et al. 2015b). The eRBs extend up to $\sim 80^{\circ}$ and are dominated by thermal X-ray emission. In the last decade,

most of the literature suggested that the FBs and eRBs were formed by 1-10 Myr past Galactic Center (GC) burst-like activities (e.g., Bland-Hawthorn et al. 2019; Yang et al. 2022; Nguyen & Thompson 2022; Owen & Yang 2022; Sarkar et al. 2023; Sarkar 2024, , for recent studies), implying that the bubbles are evanescent structures of the Milky Way Galaxy (MW). However, the true formation mechanisms are still unknown.

Linearly polarized radio observations have also reported such bilobal giant structures (Carretti et al. 2013, hereafter Giant Radio Lobes, GRLs). Several bright filamentary substructures in the GRLs trace the corresponding parts of the FBs and eRBs very well. The polarization observations also show that the magnetic fields above and below the Galactic disk are perpendicular to the disk everywhere. These facts strongly support the existence of outflows from the disk, however, the filamentary substructures may rule out a simple bubble-like morphology of the outflow.

The outflow from the Galactic disk is also strongly motivated to explain the total amount of metals in the current disk, $\sim 10^7 M_{\odot}$, which is estimated with the

typical metallicity of $Z_{\odot} \sim 0.01$ and the total mass of gaseous matter within the star-forming region of the disk $\sim 10^9 M_{\odot}$ (e.g., Misiriotis et al. 2006). Without the outflow from the Galactic disk, the metal amount would be much larger than the above estimate; The star formation in the MW has continued at a rate of $\dot{M}_{\text{sf}} \gtrsim 3 M_{\odot} \text{ yr}^{-1}$ during the cosmic-age of $t_{\text{age}} \sim 14 \text{ Gyr}$ (Haywood et al. 2016). The Salpeter initial mass function (IMF) gives a fraction of massive stars as $f_{\text{ms}} \sim 0.1$ (e.g., Kroupa 2001; Chabrier 2003). From the ratio of the metal mass of the supernova ejecta to the mass of the progenitor star as $f_{\text{ej}} \sim 0.1$ (e.g., Sukhbold et al. 2018; Chieffi & Limongi 2020), we obtain the total mass of metals ejected by the supernovae during the cosmic-age as $M_Z \sim f_{\text{ej}} f_{\text{ms}} \dot{M}_{\text{sf}} t_{\text{age}} \gtrsim 4 \times 10^8 M_{\odot} \gg 10^7 M_{\odot}$. Thus, $\gtrsim 97\%$ of the ejected metals should be removed from the disk by the outflow (Shimoda et al. 2024). The observed mid-infrared large structure around the GC (Bland-Hawthorn & Cohen 2003) may be the evidence of the outflow that removes ‘missing’ metals.

The diffuse X-ray emission from hot gaseous matter with a temperature of $\sim 0.3 \text{ keV}$ including the eRBs (e.g., Kataoka et al. 2018) may ensure the existence of the outflow from the disk, however, the origin of such diffuse X-ray emission is a long-standing problem (e.g., Koyama 2018, reviews for the emission from the disk). The possible existence of the Galactic wind driven by cosmic rays (CRs) was pointed out by Breitschwerdt et al. (1991) for the first time. Breitschwerdt & Schmutzler (1999) included the effects of the radiative cooling into the wind model and showed that the observed diffuse X-ray spectrum can be explained by the wind scenario. Everett et al. (2008, 2010) also showed that the surface brightness profile can be fitted by the successful wind model.

However, considering the cooling and CR effects with the realistic boundary condition, the geometrical structure of the Galactic wind may be complicated. The idealized solution of successful outflow could not apply to the entire region above the Galactic disks. From observed OVI absorption lines, Shapiro & Field (1976) suggested the galactic fountain flow, in which ejected hot gases above the disk cool radiatively and fall onto the disk. They estimated the scale height of the fountain flow to be $\sim 1 \text{ kpc}$, which is too small to explain the eRBs. Shimoda & Inutsuka (2022) pointed out that the heating rate due to cosmic rays (CRs) can be comparable to the radiative cooling rate for tenuous gas, and the gas can escape from the Galaxy as the Galactic wind, whose number density and temperature are $\sim 10^3 \text{ cm}^{-3}$ and $\sim 0.3 \text{ keV}$, respectively.

The wind model should be consistent with the star formation activity. With the CR-driven wind scenario of Shimoda & Inutsuka (2022), in which both the cooling and CR diffusion effects are included, Shimoda et al. (2024) reproduced the long-term evolution of the MW over cosmic time consistently with the star formation rate (SFR) and metallicity, taking into account the CR heating and stellar dynamics. They found that the MW history can be self-consistently explained if $\sim 5\text{-}10\%$ of the supernova explosion energy is used to drive the wind. Gupta et al. (2023) reported that the metal abundance of the eRBs can be consistent with the metal enrichment scenario by supernovae/stellar winds.

As discussed in Armillotta et al. (2024) for example, dense cold clouds falling onto the disk and hot gases launched from the disk coexist in the Galactic halo. Motivated by the complicated structure of the wind and fountain flow with CRs, we study the X-ray and hadronic gamma-ray emissions from the Galactic halo region without a short and intense activity of the Galactic center in this paper. Being difficult to establish a fully self-consistent model, as a first step, we adopt simplified schemes to calculate the Galactic wind motion and CR distribution to roughly reproduce the Fermi and eROSITA bubbles.

This paper is organized as follows: In Section 2, we describe our model based on the long-term evolution model and observations of the MW. The numerical results of our model are presented in Section 3. The thermal X-ray and hadronic gamma-ray emissions from the Galactic halo are reproduced. The implications of our scenario for future studies are discussed in Section 4.

2. MODEL DESCRIPTION

To produce the sky intensity maps of the hadronic gamma-ray and thermal X-ray photons, we consider the recent $\sim 1 \text{ Gyr}$ evolution of the MW according to the latest Galactic evolution model by Shimoda et al. (2024). The Galactic system is modeled under the approximation of axial symmetry with the cylindrical coordinate of (R, z) . The SFR at the disk is estimated from the disk gas distribution based on the HI and H_2 observations (Misiriotis et al. 2006). The CR energy density is estimated from the supernova rate with the Salpeter IMF (e.g., Kroupa 2001; Chabrier 2003). The outflow dynamics is regulated by the Galactic gravitational potential due to stars (Miyamoto & Nagai 1975) and the NFW-like dark matter (DM) distribution (Navarro et al. 1996). The details of our method are as follows.

2.1. the Galactic disk

We model the disk gas surface mass density following Misiriotis et al. (2006). The HI gas surface density is

$$\Sigma_{\text{HI}} = \Sigma_{0,\text{HI}} \exp \left[-\frac{R}{R_{\text{HI}}} - \left(\frac{R_t}{R} \right)^4 \right], \quad (1)$$

where $R_{\text{HI}} = 18.24$ kpc, $R_t = 2.75$ kpc, and the normalization factor of $\Sigma_{0,\text{HI}}$ is adjusted to satisfy that the enclosed mass within $R = 30$ kpc is $3.9 \times 10^9 M_\odot$ (the mass within $R = \infty$ is $8.2 \times 10^9 M_\odot$). Here we modify the cut-off shape as $\exp[-(R_t/R)^4]$ from a discontinuous cut-off originally assumed to keep its differential finite. The H_2 gas surface density is given by

$$\Sigma_{\text{H}_2}(R) = \Sigma_{0,\text{H}_2} \exp \left[-\frac{R}{R_{\text{H}_2}} \right], \quad (2)$$

where $R_{\text{H}_2} = 2.57$ kpc and the enclosed mass within $R = 30$ kpc is $1.3 \times 10^9 M_\odot$. As stars are formed in molecular clouds, the surface SFR density can be written as

$$\dot{\Sigma}_{\text{sf}}(R) = \frac{\Sigma_{\text{H}_2}}{\tau_{\text{sf}}}, \quad (3)$$

where the effective gas consumption timescale due to the star formation is assumed as $\tau_{\text{sf}} = 0.5$ Gyr (see, Inutsuka et al. 2015, for details). Figure 1 shows the surface densities of Σ_{HI} , Σ_{H_2} , $\Sigma \equiv \Sigma_{\text{HI}} + \Sigma_{\text{H}_2}$, and the enclosed SFR, $2\pi \int_0^R \dot{\Sigma}_{\text{sf}}(R') R' dR'$. The total SFR within $R = 30$ kpc becomes $2.76 M_\odot \text{ yr}^{-1}$, which is consistent with the SFR in the MW averaged for recent ~ 1 Gyr (Haywood et al. 2016).

In our model, the supernova explosions blow the gas off the disk. The event rate density of supernovae is

$$\dot{N}_{\text{sn}}(R) = f_{\text{ms}} \frac{\dot{\Sigma}_{\text{sf}}(R)}{\bar{m}_{*,\text{ms}}}, \quad (4)$$

where the Salpeter IMF provides the average mass of supernova progenitors $\bar{m}_{*,\text{ms}} = 30.9 M_\odot$ and the fraction of supernova progenitor stars $f_{\text{ms}} = 0.22$ (see, Shimoda et al. 2024, for details). A fraction of the supernova explosion energy is converted to the outflow energy so that the surface density of the outflow rate $\dot{\Sigma}_{\text{blown}}$ satisfies

$$\frac{kT_w}{m_p} \dot{\Sigma}_{\text{blown}}(R) = \eta_{\text{blown}} E_{\text{sn}} \dot{N}_{\text{sn}}(R), \quad (5)$$

where $\eta_{\text{blown}} = 0.05$ is the outflow conversion efficiency, the supernova explosion energy $E_{\text{sn}} = 10^{51}$ erg, the assumed temperature of the outflow gas $T_w = 3 \times 10^6$ K (e.g., Kataoka et al. 2013; Nakashima et al. 2018; Shimoda & Inutsuka 2022), m_p is the proton mass, and

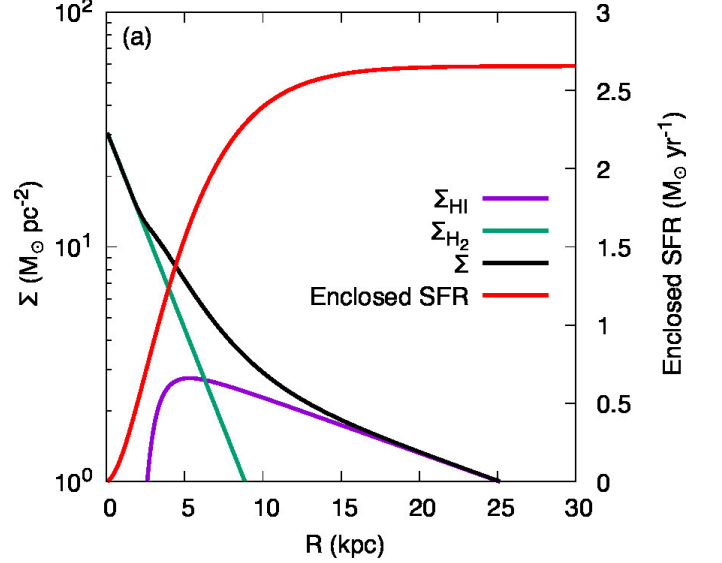


Figure 1. The surface mass density profiles of $\Sigma_{\text{HI}}(R)$, $\Sigma_{\text{H}_2}(R)$, and $\Sigma(R) \equiv \Sigma_{\text{HI}} + \Sigma_{\text{H}_2}$ (the left-hand side vertical axis). The enclosed SFR, $2\pi \int_0^R \dot{\Sigma}_{\text{sf}}(R') R' dR'$, is also shown (the right-hand side vertical axis).

k_B is the Boltzmann constant. As a result, the outflow rate from the disk can be written as $\dot{\Sigma}_{\text{blown}} = \eta_w f_{\text{ms}} \dot{\Sigma}_{\text{sf}}$, where $\eta_w \equiv \eta_{\text{blown}} m_p E_{\text{sn}} / (\bar{m}_{*,\text{ms}} k_B T_w) \simeq 3.3$.

We assume that the blown gas extends with a scale height of $z_{\text{hl}} = 2$ kpc, which corresponds to the height estimated in the classical galactic fountain scenario (Shapiro & Field 1976). In our model, the fountain regions are laid on the disk with the thickness of z_{hl} and treated separately from the disk region with the thickness of $H = 0.3$ kpc. We refer to the fountain region as the layer in the following. The gas in the layer is assumed to escape as the wind from a height of $z = z_{\text{hl}}$ with a speed of $C_{s,w} = \sqrt{k_B T_w / (\mu m_p)} \simeq 200 \text{ km s}^{-1} (T_w / 3 \times 10^6 \text{ K})^{1/2}$ to the halo, where $\mu = 0.6$ is the mean molecular weight. Then, the density of the wind is given under the steady-state approximation as

$$\rho_w(R, z_{\text{hl}}) = \frac{\eta_w f_{\text{ms}} \dot{\Sigma}_{\text{sf}}(R)}{2C_{s,w}}, \quad (6)$$

where the factor of 2 in the denominator represents the two layers existing above and below the disk. The typical number density of the wind becomes

$$n_w \equiv \rho_w / m_p \simeq 0.4 \times 10^{-3} \text{ cm}^{-3} \left(\frac{\Sigma_{\text{H}_2}}{10 M_\odot \text{ pc}^{-2}} \right), \quad (7)$$

where $\dot{\Sigma}_{\text{sf}} = \Sigma_{\text{H}_2} / \tau_{\text{sf}}$ is used. The density is consistent with the observed diffuse thermal X-rays under the assumed temperature of $k_B T_w \simeq 0.3$ keV. Note that the crossing time of the blown gas over the layer, $z_{\text{hl}} / C_{s,w} \simeq 10$ Myr, and $n_w \simeq 0.4 \times 10^{-3} \text{ cm}^{-3}$ may give

ionization states of the thermal X-ray emission consistent with the observation (Yamamoto et al. 2022).

2.2. the Galactic cosmic rays

The blown gas can be accelerated by the CR pressure and extend to a region of $z > z_{\text{hl}}$. In this paper, we mainly focus on relatively low-energy (\sim GeV) CRs, which dominate the CR energy density.

The CR transport equation is simply written as

$$\frac{\partial \mathcal{N}_{\text{cr}}(\mathbf{r}, \gamma)}{\partial t} = \dot{\mathcal{N}}_{\text{cr},s}(\mathbf{r}, \gamma) + \mathcal{D}_{\text{cr}}(\gamma) \nabla^2 \mathcal{N}_{\text{cr}}(\mathbf{r}, \gamma), \quad (8)$$

where $\mathcal{D}_{\text{cr}}(\gamma)$ is a diffusion coefficient of CRs and γ is the Lorentz factor of CRs, respectively. The CR injection rate density $\dot{\mathcal{N}}_{\text{cr},s}$ is discussed later. For simplification, here we neglect the CR advection, momentum diffusion, and non-trivial interaction with the background fluid. The fully self-consistent treatment for those effects has not been well established yet, though, several recent attempts have developed the numerical scheme (e.g. Girichidis et al. 2020, 2022, 2024; Thomas et al. 2023). As will be shown later, our treatment results in a soft CR spectrum. However, maintaining the total energy budget regulated by the star formation activities, we mainly focus on the 1 GeV gamma-ray brightness below. The caveats for the adopted simplification in our method will be discussed in Section 4. We also discuss the effects of advection in the appendix A.

With the steady-state approximation, the formal solution for the CR density \mathcal{N}_{cr} becomes

$$\mathcal{N}_{\text{cr}}(\mathbf{r}, \gamma) \approx \frac{\tau_{\text{cr}}(\gamma)}{4\pi H^2} \int \frac{\dot{\mathcal{N}}_{\text{cr},s}(\mathbf{r}', \gamma)}{|\mathbf{r} - \mathbf{r}'|} d^3 \mathbf{r}', \quad (9)$$

where $\tau_{\text{cr}} = H^2/\mathcal{D}_{\text{cr}}(\gamma)$ is the residence time of CR at the disk (the appendix A). The CR composition of unstable radioactive isotopes such as Be^{10} implies that the residence time of the low-energy CRs is ~ 1 Myr (e.g., Gabici et al. 2019, for recent reviews). In this paper, we assume the residence time as

$$\tau_{\text{cr}} = 1 \text{ Myr} \left(\frac{\gamma}{2} \right)^{-0.6}, \quad (10)$$

for simplicity, which is equivalently $\mathcal{D}_{\text{cr}} \simeq 2.7 \times 10^{28} \text{ cm}^2 \text{ s}^{-1} (\gamma/2)^{0.6} (H/0.3 \text{ kpc})^2$. The CR injection rate density is defined as

$$\dot{\mathcal{N}}_{\text{cr},s} = \dot{\mathcal{N}}_0 \left(\frac{\gamma}{2} \right)^{-2.1} \quad (\gamma \geq 2), \quad (11)$$

where the normalization factor is given by the energy injection rate density as $\dot{e}_{\text{cr},s} = \int_2^\infty \dot{\mathcal{N}}_{\text{cr},s} \gamma m_p c^2 d\gamma$, where c is the speed of light. In equation (8), we neglect the energy loss due to pp -collision, whose timescale can be estimated as $1/(K_{pp} n \sigma_{\text{hc}}) \sim 100 \text{ Myr} (n/1 \text{ cm}^{-3})^{-1}$ (e.g.,

Schlickeiser 2002), where the inelasticity $K_{pp} \sim 0.3$ and $\sigma_{\text{h}} \sim 3 \times 10^{-26} \text{ cm}^2$ is used. The energy injection rate density is obtained from the supernova rate as

$$\dot{e}_{\text{cr},s} = \frac{\eta_{\text{cr}} E_{\text{sn}}}{\bar{m}_{*,\text{ms}}} \dot{\Sigma}_{\text{sn}}(R) \delta(z), \quad (12)$$

where the CR injection efficiency is $\eta_{\text{cr}} = 0.1$, and $\delta(z)$ is the Dirac's delta function. The CR energy density and pressure are given by $e_{\text{cr}}(R, z) = \int_2^\infty \mathcal{N}_{\text{cr}} \gamma m_p c^2 d\gamma$ and $P_{\text{cr}} = e_{\text{cr}}/3$, respectively.

Our steady solution results in $\mathcal{N}_{\text{cr}} \propto \gamma^{-2.7}$ everywhere and the spectral index of -2.7 is consistent with the observed CR energy distribution around the Earth (e.g. one of the latest results: Adriani et al. 2022). Figure 2 shows the calculated CR energy density in the Galactic halo. The energy density at $R \simeq 8.5 \text{ kpc}$ is $\simeq 0.8 \text{ eV cm}^{-3}$, which agrees with the observed energy density around the Earth.

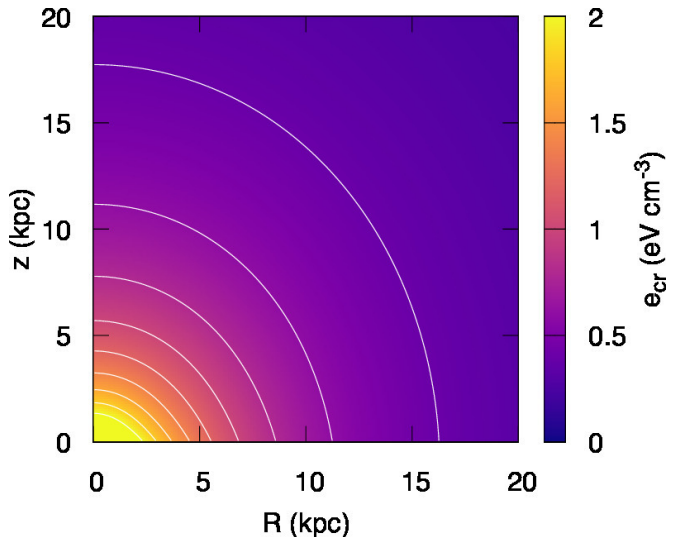


Figure 2. The CR energy density in the Galactic halo. The contours show the density increasing by 0.2 eV cm^{-3} from 0.4 eV cm^{-3} to 2.0 eV cm^{-3} .

2.3. the Galactic halo

Here we describe our model for the Galactic wind dynamics. The observed halo gas consists of hot, tenuous X-ray emitting gas (e.g., Predehl et al. 2020) and cold, dense HI clouds (e.g., Wakker & van Woerden 1997). The gas dynamics should obey highly nonlinear processes as seen in the interstellar medium (ISM, e.g., Koyama & Inutsuka 2002). To describe their dynamics precisely, we should take into account the nonlinear processes of magnetohydrodynamics by including the effects of CRs, ionization structure, thermal conduction, radiative cooling, heating process, and so on.

While the full numerical simulations of the halo winds require a high computational cost (e.g., Tan et al. 2023; Tan & Fielding 2024; Armillotta et al. 2024), the global structure of the halo gas we are interested in mainly depends on the pressure balance among gravity, CR pressure, and magnetic pressure (e.g., Boulares & Cox 1990; Ferrière 2001).

Shimoda & Inutsuka (2022) studied the effects of CRs for launching the Galactic wind and found that only when the temperature of the wind gas is kept high by the CR heating, the wind is successfully launched. In the Galactic halo, the gas heating rate due to the dissipation of Alfvén waves induced by CRs, $Q_w = V_A |\nabla P_{\text{cr}}|$, can be comparable to the radiative cooling rate of $n_w^2 \Lambda$;

$$\frac{n_w^2 \Lambda}{Q_w} \simeq 0.9 \left(\frac{n_w}{10^{-3} \text{ cm}^{-3}} \right)^{5/2} \left(\frac{\Lambda}{10^{-22} \text{ erg cm}^3 \text{ s}^{-1}} \right) \left(\frac{B}{1 \mu\text{G}} \right)^{-1} \left(\frac{e_{\text{cr}}}{1 \text{ eV cm}^{-3}} \right)^{-1} \left(\frac{H_{\text{cr}}}{10 \text{ kpc}} \right), \quad (13)$$

where V_A is the Alfvén velocity, and B is the magnetic field. When the CR heating rate is larger than the radiative cooling rate, the gas temperature maintains at the virial temperature, going to a larger z , and finally escaping from the Galactic system as the wind by the CR pressure.

To save the computational costs, we omit solving these cooling and heating processes, and simplify the halo gas dynamics as follows.¹ The validity of this simplification will be justified later. The equation of motion of the fluid element can be approximately written as

$$\frac{d\mathbf{v}_w}{dt} = -\frac{1}{\rho_w} \nabla P_{\text{cr}} - \mathbf{g}, \quad (14)$$

where \mathbf{v}_w and \mathbf{g} are the velocity and gravitational acceleration vectors, respectively. From the force balance along the z direction, $-\partial P_{\text{cr}}/\partial z - \rho_w g_z > 0$, the criterion density for the escaping outflow can be written as

$$n_{w,G} < 0.4 \times 10^{-3} \text{ cm}^{-3} \left(\frac{e_{\text{cr}}}{1 \text{ eV cm}^{-3}} \right) \left(\frac{H_{\text{cr}}}{10 \text{ kpc}} \right)^{-1} \left(\frac{\Sigma_*}{250 M_\odot \text{ pc}^{-2}} \right)^{-1} \quad (15)$$

where we have adopted $\partial P_{\text{cr}}/\partial z \sim -P_{\text{cr}}/H_{\text{cr}}$, and $g_z \sim 2\pi\Sigma_*$. The threshold mass density of the stellar disk is estimated as $\Sigma_* \sim M_*/(2\pi R_{*,d}^2) \sim 250 M_\odot \text{ pc}^{-2}$,

where $M_* \sim 4 \times 10^{10} M_\odot$ and $R_{*,d} \sim 5 \text{ kpc}$ (e.g., Bland-Hawthorn & Gerhard 2016). An outflow from the inner region ($R \lesssim 5 \text{ kpc}$) where the number density is larger than the above value, can not escape from the Galactic system, falling back onto the Galactic disk, similar to the Galactic fountain flow. This critical density is close to the critical density for the cooling effect shown in eq. (13). Therefore, our method with eq. (14) can roughly reproduce the escaping wind and fallback gas without considering the cooling effect. Considering the strong density dependence of $n_w^2 \Lambda/Q_w \propto n_w^{5/2}$, we can reasonably conclude that the gas dynamics mainly depends on n_w and the CR pressure.² An outflow from $R \gtrsim 5 \text{ kpc}$ can escape from the Galactic system as the wind, but it is relatively less important for the thermal X-ray emissivity and hadronic gamma-ray emissivity.

The Galactic fountain-like flow implies the coexistence of the outflow and infalling failed wind in the halo. From the condition of $n_{w,c} \sim n_{w,G}$, we expect that the failed wind suffers the radiative cooling and becomes condensed gas due to the thermal instability (e.g., Field 1965; Shapiro & Field 1976). Such multiphase gas, in which cold, dense gas coexists with hot, diffuse gas, is ubiquitously observed in the ISM, in the MW halo (e.g., Bregman & Lloyd-Davies 2007; Das et al. 2019), and in the external galaxy's halo (e.g., Tumlinson et al. 2017, for reviews). Moreover, many HI clouds falling into the MW disk are observed (the so-called high-velocity/intermediate-velocity cloud, e.g., Wakker & van Woerden 1997). In this paper, we assume that the halo gas density is highly structured in reality and the motion of the outflowing wind is not affected by the inflowing gas (like "raindrops" in the atmosphere).

We summarize our expectations as follows. The outflow from the inner region ($R \lesssim 5 \text{ kpc}$ and $n_w \gtrsim 10^{-3} \text{ cm}^{-3}$) suffers radiative cooling and falls back onto the disk. The motion of the fluid element can be approximated by the equation (14). The outflow from the outer region ($R \gtrsim 5 \text{ kpc}$ and $n_w \lesssim 10^{-3} \text{ cm}^{-3}$) is affected by the CR heating so that the thermal pressure is large enough. However, a lower density in the outer wind may result in lower emissivities of the thermal X-ray and hadronic gamma-ray. Even if we adopt the equation (14) to their dynamics, the X-ray and gamma-ray intensities are less affected. The outflow at the critical

¹ The magnetic field strength is one of the most uncertain quantities in the Galactic halo. Even if we suppose a comparable strength to the strength at the disk as $B \sim 1 \mu\text{G}$, the plasma beta becomes $\beta \sim 10 (n_w/10^{-3} \text{ cm}^{-3}) (kT_w/0.3 \text{ keV}) (B/1 \mu\text{G})^{-2}$ and the magnetic pressure becomes $\sim 0.02 \text{ eV cm}^{-3} (B/1 \mu\text{G})^2 < P_{\text{cr}}$.

² When P_{cr} is small, the thermal pressure becomes negligible due to the radiative cooling. The cooling time scale is $\tau_{\text{cool}} \sim k_B T_w / (n_w \Lambda) \sim 160 \text{ Myr} (k_B T_w / 0.3 \text{ keV}) (n_w / 10^{-3} \text{ cm}^{-3})^{-1} (\Lambda / 10^{-22} \text{ erg cm}^3 \text{ s}^{-1})^{-1}$, while the dynamical time scale is $\tau_{\text{dyn}} \sim H_{\text{cr}} / v_w \sim 50 \text{ Myr} (H_{\text{cr}} / 10 \text{ kpc}) (v_w / 200 \text{ km s}^{-1})^{-1}$.

density $n_w \simeq 10^{-3} \text{ cm}^{-3}$ ($R \simeq 5 \text{ kpc}$) can be regarded as a minor component because of $n_{w,c} \propto n_w^{5/2}$ and the exponential profile of Σ_{H_2} (see, equations 2 and 7).

For numerical calculation of the wind, following Shimoda et al. (2024), we treat the fluid element as a test particle denoted by subscript i and adopt the equation (14) as its equation of motion under the axisymmetric approximation. We prepare the particles at (R_i, z_{hl}) , where R_i is discretized with the interval of $\Delta R = (30/256) \text{ kpc} \simeq 0.017 \text{ kpc}$. Considering the criterion for the fallback discussed above, we can simplify the estimate of the acceleration by the CR pressure using the initial density $\rho_{w,\text{hl}}(R_i, z_{\text{hl}})$. We set two spatial boundary conditions at $r = 30 \text{ kpc}$ as the free escape boundary and $z = 0.3 \text{ kpc}$, below which the wind merges with the disk gas. The initial velocity components are set to be $(v_{w,R}, v_{w,\phi}, v_{w,z}) = (0, v_{w,\phi,i}(R_i, z_{\text{hl}}), C_{s,w})$, where the initial rotation velocity $v_{w,\phi,i}$ is a free parameter in this model. We use simple formulae of the gravitational potentials due to the stars (Miyamoto & Nagai 1975) and DMs (Navarro et al. 1996) following Shimoda & Inutsuka (2022).

We have adjusted the model parameters to reproduce the current MW conditions except for the systematic rotation of the halo gas, which is currently not constrained. The angular momentum transportation is an important factor for the long-term evolution of galaxies in general. On the other hand, the angular momentum (AM) can be redistributed at the disk-halo interface by e.g., magnetic fields (Breitschwerdt & Schmutzler 1999; Kakiuchi et al. 2024), and a large-ordered field possibly regulates the outflow (Meliani et al. 2024). In this paper, we test two cases parametrizing the initial rotation velocity of the wind as $v_{w,\phi,i}(R_i, z_{\text{hl}}) = \sqrt{R_i g_R(R_i, z_{\text{hl}})}$ (co-rotating halo) and $v_{w,\phi,i}(R_i, z_{\text{hl}}) = 0.5 \sqrt{R_i g_R(R_i, z_{\text{hl}})}$ (AM redistribution case).

Figure 3 shows the trajectories of the wind particles. Assuming continuous wind ejections and steady winds, we obtain the wind density from the particle trajectories with the mass conservation and Gaussian smoothing with the width of z_{hl} . In the co-rotating halo case (Figure 3a), the centrifugal force equilibrium condition, $v_{w,\phi,i} = \sqrt{R_i g_R(R_i, z_{\text{hl}})}$, results in a simple fountain flow; the wind goes in the outward direction due to the centrifugal force and eventually falls back on the disk. In the AM redistribution case shown in Figure 3b, $v_{w,\phi,i} = 0.5 \sqrt{R_i g_R(R_i, z_{\text{hl}})}$, the wind is concentrated toward the inner Galactic region attracted by the stellar gravity. Although our treatment neglects the effects depending on B and Λ , the numerical results are consistent with our expectations discussed above.

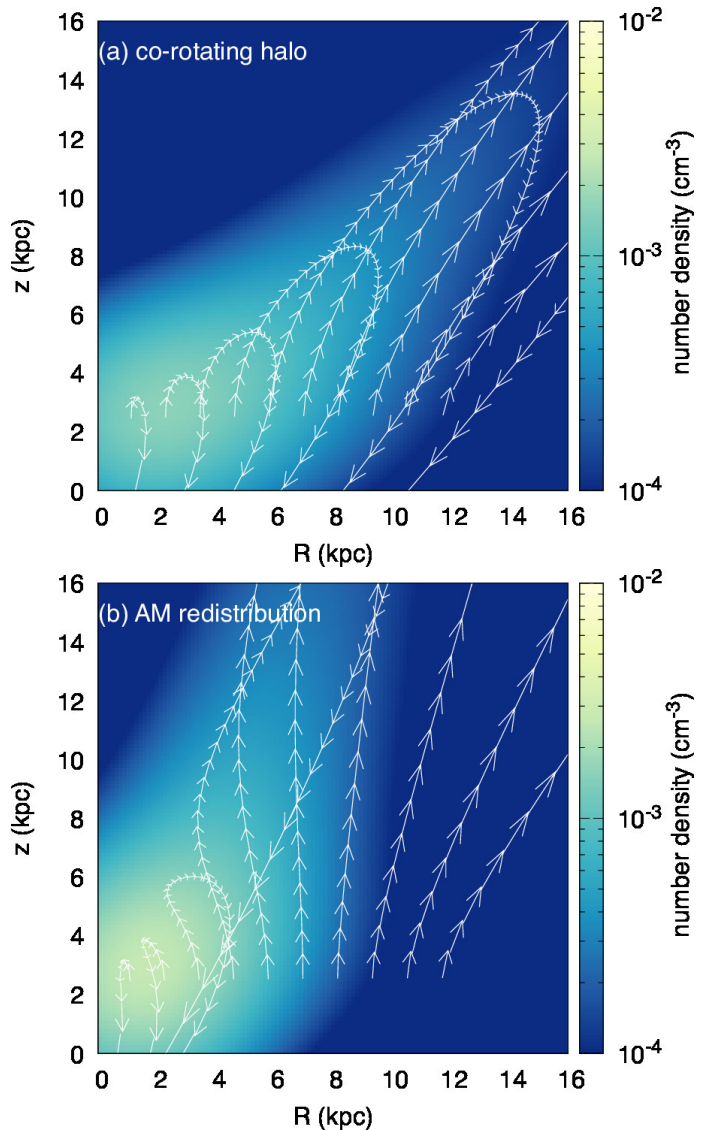


Figure 3. The trajectories of the fluid elements (vectors). The color map shows the wind density. The panels (a) and (b) show the case of $v_{w,\phi,i}(R_i, z_{\text{hl}}) = \sqrt{R_i g_R(R_i, z_{\text{hl}})}$ (co-rotating halo) and $v_{w,\phi,i}(R_i, z_{\text{hl}}) = 0.5 \sqrt{R_i g_R(R_i, z_{\text{hl}})}$ (AM redistribution), respectively.

2.4. the thermal X-rays and hadronic gamma-rays

For the thermal X-ray emission from the halo in the *eROSITA* 0.6-1 keV band, we assume an average, spatially uniform emissivity of $\Lambda_X = 10^{-23} \text{ erg cm}^3 \text{ s}^{-1}$ for simplicity. This assumption is equivalent to the isothermal gas with a temperature of $\sim 0.3 \text{ keV}$. The hadronic gamma-ray emission from CRs via pp -collision is calculated with the same method in Nishiwaki et al. (2021). For the total cross-section, we use the formulae in Kamae et al. (2006); Kamae et al. (2007). The energy distribution of π^0 produced in a collision is expressed by the formulae in Kelner et al. (2006). With

the π^0 -injection rate density $\dot{q}_\pi(E_\pi)$ obtained with the method above, the gamma-ray emissivity due to π^0 -decay is calculated as

$$\dot{\epsilon}(E_\gamma) = 2E_\gamma \int_{E_{\text{th}}} \frac{\dot{q}_\pi(E_\pi)}{\sqrt{E_\pi^2 - m_\pi^2 c^4}} dE_\pi, \quad (16)$$

where $E_{\text{th}} = E_\gamma + m_\pi^2 c^4 / (4E_\gamma)$. The intensity map is obtained by integrating the emissivity along the line of sight.

The order of magnitude estimate of the hadronic gamma-ray intensity, \mathcal{J}_γ , may be given by (Schlickeiser 2002)

$$\begin{aligned} \mathcal{J}_\gamma &\sim \frac{D}{4\pi} \frac{n_{\text{cr}} n_w \sigma_h c}{m_\pi c^2} \left[\frac{E_\gamma}{m_\pi c^2} + \frac{m_\pi c^2}{4E_\gamma} \right]^{-1.6} \\ &\sim 0.7 \times 10^{-6} \text{ ph cm}^{-2} \text{ s}^{-1} \text{ GeV}^{-1} \text{ str}^{-1} \\ &\quad \left(\frac{D}{3 \text{ kpc}} \right) \left(\frac{e_{\text{cr}}}{1 \text{ eV cm}^{-3}} \right) \\ &\quad \left(\frac{n_w}{10^{-2} \text{ cm}^{-3}} \right) \left(\frac{E_\gamma}{1 \text{ GeV}} \right)^{-1.6}, \end{aligned} \quad (17)$$

where $m_\pi = 140 \text{ MeV}$ is the pion mass, $\sigma_h \sim 10^{-26} \text{ cm}^2$ is the cross-section, D is the path length, and we use $n_{\text{cr}} \sim e_{\text{cr}}/m_p c^2$. Note that $\mathcal{J}_\gamma \propto \Sigma_{\text{sf}}^2$ in our model and the neutrino emission with a comparable intensity to \mathcal{J}_γ is also expected.

3. RESULTS

The numerical results of the thermal X-ray and hadronic gamma-ray intensities are presented here. We compare the surface brightness profiles to the actual observations and predict the line-of-sight velocity distribution of each co-rotating halo case and AM redistribution case for future radio and X-ray observations.

Figure 4 shows the surface brightness of the 1 GeV hadronic gamma-ray from the disk ($|b| < 5^\circ$). This shows that the CR density we assumed consistently reproduces the observed gamma-ray brightness at the disk (e.g., Strong et al. 2004).

As shown in Figure 3, the failed wind around the inner region may be observed as ‘bubbles’ in the X/ γ -ray sky due to the projection effect. Figure 5 shows the estimated intensity maps of the thermal X-ray and hadronic gamma-ray at $E_\gamma = 1 \text{ GeV}$. Here we only calculate the emission from the halo. The numerically computed \mathcal{J}_γ at $E_\gamma = 1 \text{ GeV}$ is consistent with the estimated intensity given by the equation (17) and the observed intensities (e.g., Su et al. 2010; Ackermann et al. 2014). The morphological relation between the eRBs and FBs is that the FBs are bright *inside* the eRBs. Such morphology is reproduced very well in both the two models for the initial rotation.

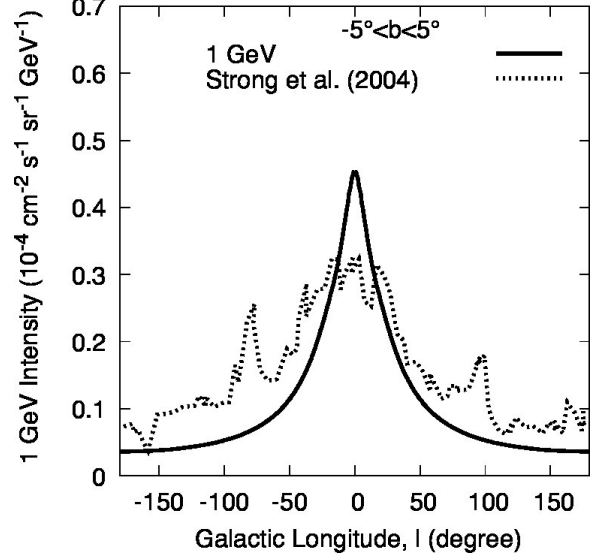


Figure 4. The surface brightness of the 1 GeV hadronic gamma-ray at the disk (solid line). The dots are derived from Strong et al. (2004) as a guide.

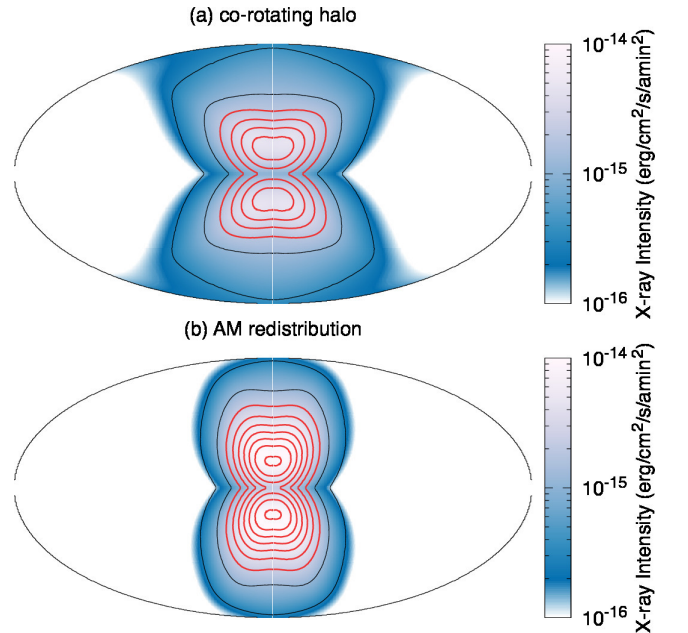


Figure 5. The intensity sky maps of the hadronic gamma-ray and X-ray observed from $(R, z) = (8.5 \text{ kpc}, 0 \text{ kpc})$. The contour shows the 1 GeV gamma-ray intensity (photon $\text{cm}^{-2} \text{ s}^{-1} \text{ str}^{-1}$) increasing by 0.25×10^{-6} from 0 to 3×10^{-6} . The red contours indicate the intensity larger than 0.5×10^{-6} . The color shows the X-ray intensity for the 0.6-1 keV band under the assumed emissivity of $n_w \Lambda_X / 4\pi$, where $\Lambda_X = 10^{-23} \text{ erg cm}^3 \text{ s}^{-1}$.

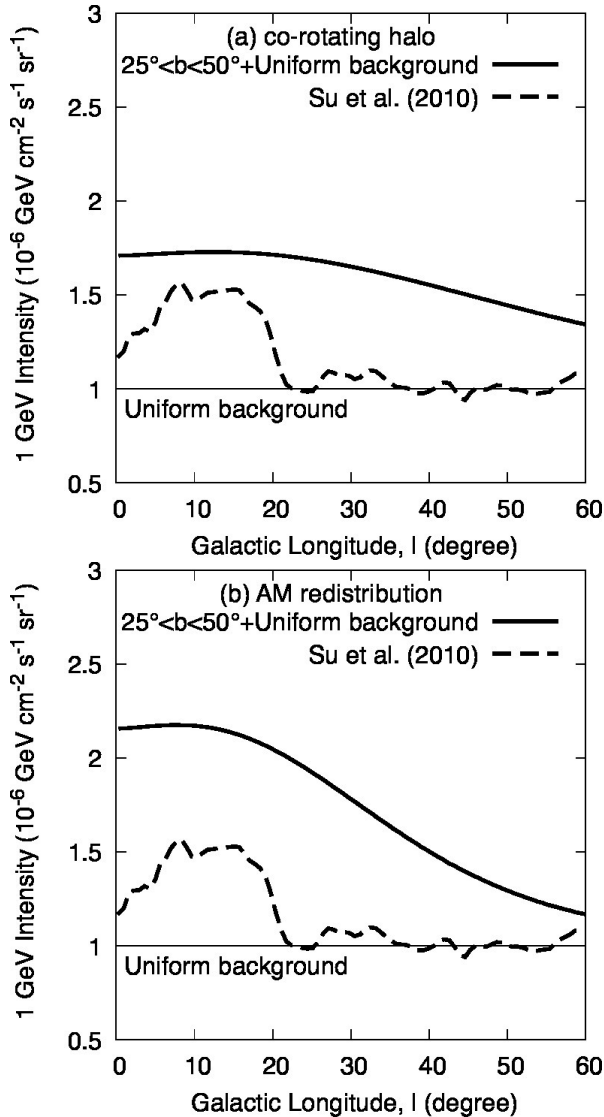


Figure 6. The surface brightness profile of the 1 GeV hadronic gamma-ray observed from $(R, z) = (8.5 \text{ kpc}, 0 \text{ kpc})$. We add the uniform background component with brightness of $10^{-6} \text{ GeV cm}^{-2} \text{ s}^{-1} \text{ sr}^{-1}$. The broken line is derived from Su et al. (2010) as a guide.

Figure 6 shows the surface brightness profile of the hadronic gamma-ray averaged on the Galactic latitude ranges of $25^\circ < b < 50^\circ$. The actual profiles of the FBs are analyzed by Su et al. (2010) (Figure 8) and Ackermann et al. (2014) (Figure 23) for examples. The surface brightness of the FBs is not perfectly symmetric; the northern bubble is ~ 2 times brighter than the southern bubble. Here we compare our results to the southern bubble where the gamma-ray foreground is fainter than the northern sky (Su et al. 2010). Our model results in consistent surface brightness with the observations. Note that our primitive model does not aim to exactly reproduce the gamma-ray flux. The dif-

ference with a factor ~ 2 does not matter in this paper. The surface brightness profile flattens at $|l| \lesssim 20^\circ$, which is one of the non-trivial features of the FBs. The AM redistribution case results in such a flat profile, while the co-rotating halo case results in a shallower profile. Thus, the AM redistribution case is favored for explaining the FBs. Compared to the observed sharp drop of the gamma-ray intensity at the edge of the FBs at $l = 20$ degree, the model intensity gradually decreases with the Galactic longitude for $l > 20$ degree.

Figure 7 shows the surface brightness profiles of the thermal X-ray at the Galactic latitudes of $b = 60^\circ$ (see, Predehl et al. 2020, for a comparison). Here we assume a uniform background with an intensity of $4 \text{ counts s}^{-1} \text{ cm}^{-2} \text{ deg}^{-2}$. Similar to the FBs, the observed surface brightness of the eRBs is not perfectly symmetric; the northern bubble is ~ 2 times brighter than the southern bubble. The surface brightness of the observed northern and southern bubbles is $\gtrsim 6 \text{ counts s}^{-1} \text{ cm}^{-2} \text{ deg}^{-2}$ at $-45^\circ \lesssim l \lesssim 65^\circ$ and shows flat profiles respecting l . The co-rotating halo case shows smaller l gradients than the observed northern bubble. The AM redistribution case may be preferred for explaining the northern bubble, while both cases are consistent with the southern bubble.

Figure 8 shows the line-of-sight velocity distribution of the fluid elements for $40^\circ < b < 80^\circ$. The azimuthal position of each wind particle is randomly selected. Here we regard that the outflow particles ($v_{z,w} > 0$) are observed at the X-ray band and that the inflow particles ($v_{z,w} < 0$) are cooled. The inflowing cold gas is assumed to be bright at the radio band (the 21 cm line emission) and observed like the high velocity/intermediate velocity HI clouds (e.g., Wakker & van Woerden 1997; Ashley et al. 2022; Hayakawa & Fukui 2022). The sample density respecting l reflects the gas angular momentum trivially; the AM redistribution case results in centrally concentrated samples. For a small longitude $l \lesssim 50^\circ$, the line-of-sight velocity at the radio band is bounded at $|v_{\text{los}}| \lesssim 100 \text{ km s}^{-1}$ in the co-rotating halo case ($|v_{\text{los}}| \lesssim 200 \text{ km s}^{-1}$ in the AM redistribution case). The probability distribution functions of the line-of-sight velocity at $40^\circ < b < 80^\circ$ and $|l| < 50^\circ$ are shown in Figure 9. The radio observations of the high-velocity clouds around the FBs reported the line-of-sight velocity range of $\sim \pm 170 \text{ km s}^{-1}$ (e.g., Ashley et al. 2022), which is consistent with the AM redistribution case. Thus, the halo gas dynamics will be tested by spectroscopy at the radio band and X-ray band. In particular, we need a high-energy-resolution X-ray spectroscopy like *XRISM* mission (Tashiro et al. 2020) and *Athena* mission (Barret et al. 2018).

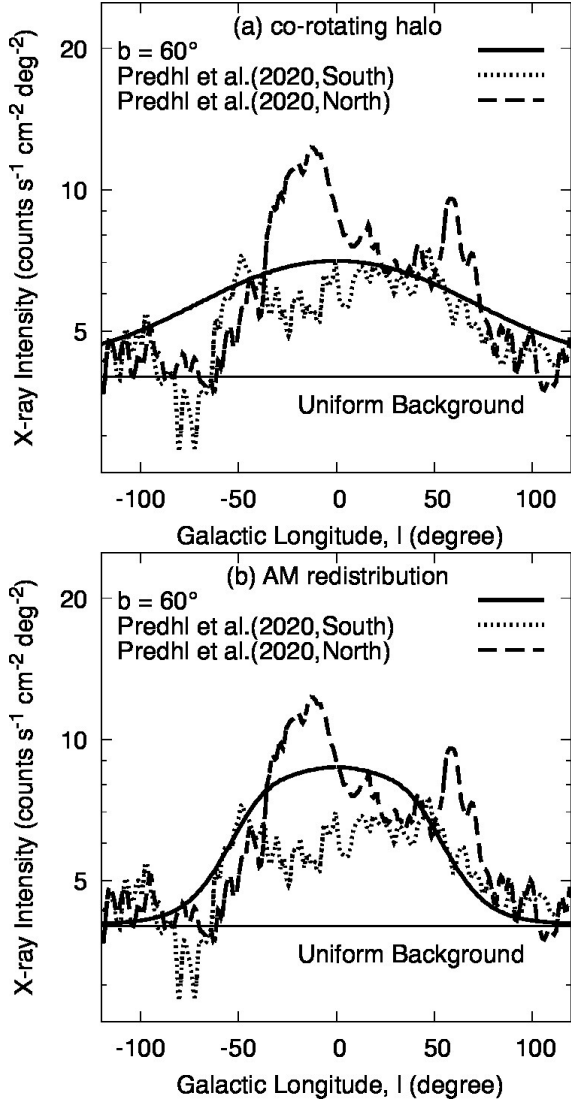


Figure 7. The surface brightness profile of the X-ray at $b = 60^\circ$ observed from $(R, z) = (8.5 \text{ kpc}, 0 \text{ kpc})$ (the solid line). The dots and the broken line are referred from [Predhl et al. \(2020\)](#) as guides for the southern and northern bubbles, respectively. The intensity is scaled as $1 \text{ counts s}^{-1} \text{ cm}^{-2} \text{ deg}^{-2} = 2.7 \times 10^{-16} \text{ erg s}^{-1} \text{ cm}^{-2} \text{ arcmin}^{-2}$ for *eROSITA* 0.6-1 keV band. We assume a uniform background with an intensity of $4 \text{ counts s}^{-1} \text{ cm}^{-2} \text{ deg}^{-2}$.

4. CONCLUSIONS AND DISCUSSION

We have shown that the eRBs and FBs can be explained by the persistent Galactic wind scenario, which is well motivated by the long-term evolution of the MW; the gas supply and consumption due to the star formation and Galactic wind are balanced, keeping the total metal content in the disk ([Shimoda et al. 2024](#)). As the computational cost for the halo dynamics simulations is high, we have modeled the gas density profile affected

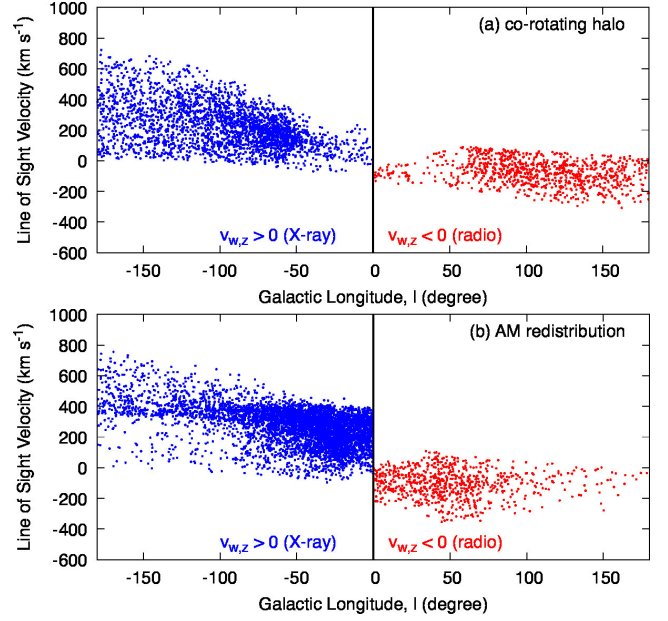


Figure 8. The line of sight velocities of the halo gas at $40^\circ < b < 80^\circ$ observed from $(R, z) = (8.5 \text{ kpc}, 0 \text{ kpc})$ under the assumed rotation velocity of the solar cycle of 230 km s^{-1} . The case $v_{w,z} < 0$ is shown at $l > 0$ and case $v_{w,z} > 0$ is shown at $l < 0$.

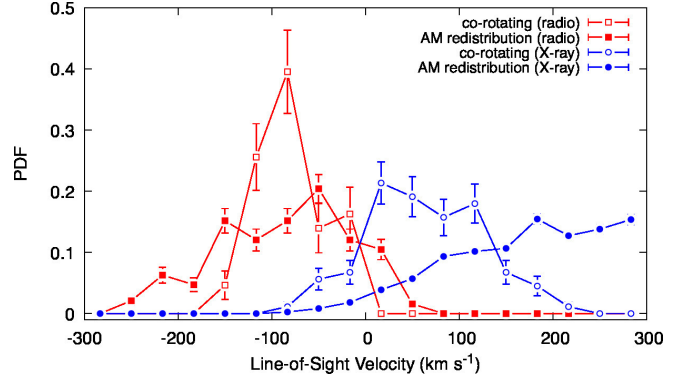


Figure 9. The probability distribution functions of the line of sight velocities of the halo gas at $40^\circ < b < 80^\circ$ and $|l| < 50^\circ$. The 1σ statistical errors due to a finite number of the samples are also shown. The unfilled (filled) circles/squares indicate the co-rotating (AM redistribution) case.

by the disk wind with a very simplified method using test particles. Despite this primitive estimate for the halo density profile, the brightness and the spatial scales of the FBs and eRBs are roughly reproduced. Especially, the non-trivial configuration, the FBs surrounded by the larger eRBs, is consistently reproduced. In addition, the velocity distribution of the inflowing gases in our model is similar to the observed velocities for high-velocity clouds. The results imply that the steady

Galactic fountain flow consistent with the star formation history in the Galactic disk produces the dense halo structure, which is responsible for both the FBs and eRBs. In this model, the FBs and eRBs are quasi-steady structures due to the quasi-steady star formation activity in the Galactic disk. The results prefer the case that the angular momentum of the wind is partially extracted by some kind of dissipative process.

On the other hand, our model does not reproduce the sharp edge of the FBs and their hard spectra. Our steady solution for the CR transport equation (8) leads to a soft gamma-ray spectrum as $\mathcal{J}_\gamma \propto E_\gamma^{-1.6}$ everywhere, although the spectra of the FBs are as hard as $\propto E_\gamma^{-1}$. The coexistence of the outflowing hot gas and infalling cold gas in the halo implies hydrodynamical instabilities. A detailed modeling with the effects of such instabilities may improve the results. If we consider the re-acceleration mechanism such as the stochastic acceleration by turbulence, the hard spectrum can be reproduced. In our AM redistribution case, the halo gas is concentrated towards the inner halo region. Thus, the inner region can be selectively disturbed, and we naturally expect an efficient re-acceleration.

The stochastic acceleration can also re-accelerate CR electrons (see e.g. Schlickeiser 1989; Brunetti & Lazarian 2011; Teraki & Asano 2019). CR electrons in the Galactic halo should be responsible for the bright GRLs. If the re-acceleration of electrons works very well, the leptonic gamma-ray emission can be comparably bright with the FBs (e.g., Sasaki et al. 2015). The efficiency of the re-acceleration can be tested by observing a hard X-ray synchrotron emission, although there is only an upper limit on the hard X-ray intensity for the Galactic halo (e.g., Kataoka et al. 2013, 2018). Thus, further studies for the re-acceleration and observations at the hard X-ray band like *FORCE* mission (Mori et al. 2022) are ideal. It should be emphasized that observations of the FBs at the very high energy gamma-ray band by, e.g., the *Cherenkov Telescope Array Observatory* and of neutrinos by, e.g., the *IceCube* experiment, are also important to reveal the maximum

energy of CRs and to verify the hadronic/leptonic scenarios (e.g., acceleration efficiency ratio of CR protons to CR electrons, see, Nishiwaki et al. 2021).

Carretti et al. (2013) estimated the magnetic energy of the GRLs with the leptonic scenario for the gamma-ray intensity as $U_{B,\text{lobe}} \sim 10^{55}$ erg. This is comparable to the energy in the disk within the active star formation region; $U_{B,\text{disk}} \sim (B^2/8\pi) \times 2\pi R^2 H \sim 10^{55} \text{ erg} (B/1 \mu\text{G})^2 (R/5 \text{ kpc})^2 (H/300 \text{ pc})$. In our scenario, the plasma circulates through the disk and the halo. Therefore, the comparable magnetic energy may be acceptable. Note that even if the magnetic reconnection dissipates the magnetic energy, which is one of the possible origins of the AM redistribution, the halo gas concentration can be responsible for the turbulent dynamo at the halo. This should be studied with stochastic acceleration.

The morphology of the eRBs and FBs depends on the angular momentum of the halo gas in our model. These are new important clues to study the long-term evolution of the MW on the time scale of ~ 1 Gyr. Since the angular momentum of the disk gas is recorded to the formed stars, the evolution of the angular momentum can be studied through the stellar dynamics. Thus, there is a possible synergy between high-energy astrophysics, CR physics, and the Galactic archaeological study of stellar dynamics. We will extend our model along the lines of this study.

ACKNOWLEDGMENTS

The authors thank S.-i. Inutsuka and M. Nagashima for fruitful discussions. We also thank the anonymous referee, for his/her comments that further improved the paper. This work is supported by the joint research program of the Institute for Cosmic Ray Research (ICRR), the University of Tokyo, and KAKENHI grant Nos. 22K03684, 23H04899, 24H00025 (K.A.), and 24K00677 (J.S.).

APPENDIX

A. THE ADVECTION EFFECTS ON THE CR TRANSPORTATION

We evaluate the effects of advection, which is neglected in the CR transport equation (8). As discussed Sections 2.3 and 4, the expected velocity field consists of inflows and outflows, having a highly complicated structure in reality. Such a velocity field cannot be treated fully consistently by our two-dimensional model, in which all values are averaged out in the azimuthal angle direction. To check the validity or limit of our treatment, we consider an extreme case with a constant velocity field along the vertical direction, $\mathbf{v} = (0, 0, v_0)$ ($z > 0$), which maximizes the advection effect.

Then, the transport equation becomes

$$\frac{\partial \mathcal{N}_{\text{cr}}}{\partial t} = \dot{\mathcal{N}}_{\text{cr},s} + \mathcal{D}_{\text{cr}}(\gamma) \nabla^2 \mathcal{N}_{\text{cr}} - v_0 \frac{\partial \mathcal{N}_{\text{cr}}}{\partial z}, \quad (\text{A1})$$

and its formal solution can be derived using the Green function as

$$\mathcal{N}_{\text{cr}}(t, \mathbf{r}, \gamma) = \frac{1}{8(\pi \mathcal{D}_{\text{cr}})^{3/2}} \int d^3 \mathbf{r}' \int_{t_0}^t dt' \frac{\dot{\mathcal{N}}_{\text{cr},s}(\mathbf{r}')}{(t-t')^{3/2}} \exp \left[-\frac{(x-x')^2 + (y-y')^2 + \{(z-z') - v_0(t-t')\}^2}{4\mathcal{D}_{\text{cr}}(t-t')} \right]. \quad (\text{A2})$$

Introducing a variable $w = \sqrt{\mathcal{T}_{\text{ad}}/(t-t')}$, where $\mathcal{T}_{\text{ad}} = 4\mathcal{D}_{\text{cr}}/v_0^2$, we obtain

$$\mathcal{N}_{\text{cr}}(t, \mathbf{r}, \gamma) = \frac{1}{4(\pi \mathcal{D}_{\text{cr}})^{3/2}} \int d^3 \mathbf{r}' \dot{\mathcal{N}}_{\text{cr},s}(\mathbf{r}') \int_{w_0}^{\infty} \frac{dw}{\mathcal{T}_{\text{ad}}^{1/2}} \exp \left[-aw^2 - \frac{1}{w^2} + \frac{2h}{v_0 \mathcal{T}_{\text{ad}}} \right], \quad (\text{A3})$$

where $h = z - z'$, $a = |\mathbf{r} - \mathbf{r}'|^2 / (4\mathcal{D}_{\text{cr}} \mathcal{T}_{\text{ad}})$, and $w_0 = \sqrt{\mathcal{T}_{\text{ad}}/(t-t_0)}$, respectively. Since the advection time scale, $\mathcal{T}_{\text{ad}} \sim 10 \text{ Myr}(\gamma/2)^{0.6} (v_0/C_{s,w})^{-2}$ with $C_{s,w} = 200 \text{ km s}^{-1}$, is significantly shorter than $(t-t_0) \gtrsim 1 \text{ Gyr}$, we can approximate $w_0 \approx 0$. Then, the integration of w is carried out by the Gaussian integral (or the Euler-Poisson integral) as

$$\mathcal{N}_{\text{cr}}(\mathbf{r}, \gamma) \approx \frac{\tau_{\text{cr}}(\gamma)}{4\pi H^2} \int d^3 \mathbf{r}' \frac{\dot{\mathcal{N}}_{\text{cr},s}(\mathbf{r}')}{|\mathbf{r} - \mathbf{r}'|} \exp \left[-\frac{|\mathbf{r} - \mathbf{r}'| - 2(z-z')}{\mathcal{H}_{\text{ad}}(\gamma)} \right], \quad (\text{A4})$$

where $\mathcal{D}_{\text{cr}}(\gamma) = H^2/\tau_{\text{cr}}(\gamma)$ is used (see the main text), and $\mathcal{H}_{\text{ad}}(\gamma) = 4\mathcal{D}_{\text{cr}}(\gamma)/v_0 \sim 2 \text{ kpc} (\gamma/2)^{0.6} (v_0/C_{s,w})^{-1}$ is the scale height of the advection. Compared with a pure diffusion case of the equation (9), the last exponential factor in the equation (A4) indicates the correction by the advection term. When $|\mathbf{r} - \mathbf{r}'| \ll \mathcal{H}_{\text{ad}}$, the factor can be reduced as unity, and we obtain the equation (9). This means that a contribution of a source at $\mathbf{r}' = (x', y', 0)$ for a CR number density at a position of $\mathbf{r} = (x, y, z)$ is mostly determined by diffusion. Our model focuses on $\sim 1 \text{ GeV}$ gamma-rays emitted by CRs with $\gamma \sim 20$. In this case, $\mathcal{H}_{\text{ad}} \sim 8 \text{ kpc}$ is significantly large even in this extreme/simplified setup for the velocity field. The transport equation (8) may not lead to a largely different CR density around the GC within a radius of $\lesssim 8 \text{ kpc}$, which is compatible with the size of the FBs. As discussed in Section 4, the effects of a realistic, turbulent velocity field will be studied in future work.

REFERENCES

- Ackermann, M., Albert, A., Atwood, W. B., et al. 2014, *ApJ*, 793, 64, doi: [10.1088/0004-637X/793/1/64](https://doi.org/10.1088/0004-637X/793/1/64)
- Adriani, O., Akaike, Y., Asano, K., et al. 2022, *PhRvL*, 129, 101102, doi: [10.1103/PhysRevLett.129.101102](https://doi.org/10.1103/PhysRevLett.129.101102)
- Armillotta, L., Ostriker, E. C., Kim, C.-G., & Jiang, Y.-F. 2024, *ApJ*, 964, 99, doi: [10.3847/1538-4357/ad1e5c](https://doi.org/10.3847/1538-4357/ad1e5c)
- Ashley, T., Fox, A. J., Cashman, F. H., et al. 2022, *Nature Astronomy*, 6, 968, doi: [10.1038/s41550-022-01720-0](https://doi.org/10.1038/s41550-022-01720-0)
- Barret, D., Lam Trong, T., den Herder, J.-W., et al. 2018, in *Society of Photo-Optical Instrumentation Engineers (SPIE) Conference Series*, Vol. 10699, *Space Telescopes and Instrumentation 2018: Ultraviolet to Gamma Ray*, ed. J.-W. A. den Herder, S. Nikzad, & K. Nakazawa, 106991G, doi: [10.1117/12.2312409](https://doi.org/10.1117/12.2312409)
- Bland-Hawthorn, J., & Cohen, M. 2003, *ApJ*, 582, 246, doi: [10.1086/344573](https://doi.org/10.1086/344573)
- Bland-Hawthorn, J., & Gerhard, O. 2016, *ARA&A*, 54, 529, doi: [10.1146/annurev-astro-081915-023441](https://doi.org/10.1146/annurev-astro-081915-023441)
- Bland-Hawthorn, J., Maloney, P. R., Sutherland, R., et al. 2019, *ApJ*, 886, 45, doi: [10.3847/1538-4357/ab44c8](https://doi.org/10.3847/1538-4357/ab44c8)
- Boulares, A., & Cox, D. P. 1990, *ApJ*, 365, 544, doi: [10.1086/169509](https://doi.org/10.1086/169509)
- Bregman, J. N., & Lloyd-Davies, E. J. 2007, *ApJ*, 669, 990, doi: [10.1086/521321](https://doi.org/10.1086/521321)
- Breitschwerdt, D., McKenzie, J. F., & Voelk, H. J. 1991, *A&A*, 245, 79
- Breitschwerdt, D., & Schmutzler, T. 1999, *A&A*, 347, 650, <https://arxiv.org/abs/astro-ph/9902268>
- Brunetti, G., & Lazarian, A. 2011, *MNRAS*, 412, 817, doi: [10.1111/j.1365-2966.2010.17937.x](https://doi.org/10.1111/j.1365-2966.2010.17937.x)
- Carretti, E., Crocker, R. M., Staveley-Smith, L., et al. 2013, *Nature*, 493, 66, doi: [10.1038/nature11734](https://doi.org/10.1038/nature11734)
- Chabrier, G. 2003, *PASP*, 115, 763, doi: [10.1086/376392](https://doi.org/10.1086/376392)
- Cheng, K. S., Chernyshov, D. O., Dogiel, V. A., & Ko, C. M. 2014, *ApJ*, 790, 23, doi: [10.1088/0004-637X/790/1/23](https://doi.org/10.1088/0004-637X/790/1/23)

- . 2015a, *ApJ*, 804, 135,
doi: [10.1088/0004-637X/804/2/135](https://doi.org/10.1088/0004-637X/804/2/135)
- . 2015b, *ApJ*, 799, 112,
doi: [10.1088/0004-637X/799/1/112](https://doi.org/10.1088/0004-637X/799/1/112)
- Cheng, K. S., Chernyshov, D. O., Dogiel, V. A., Ko, C. M., & Ip, W. H. 2011, *ApJL*, 731, L17,
doi: [10.1088/2041-8205/731/1/L17](https://doi.org/10.1088/2041-8205/731/1/L17)
- Chieffi, A., & Limongi, M. 2020, *ApJ*, 890, 43,
doi: [10.3847/1538-4357/ab6739](https://doi.org/10.3847/1538-4357/ab6739)
- Crocker, R. M., & Aharonian, F. 2011, *PhRvL*, 106, 101102, doi: [10.1103/PhysRevLett.106.101102](https://doi.org/10.1103/PhysRevLett.106.101102)
- Crocker, R. M., Bicknell, G. V., Taylor, A. M., & Carretti, E. 2015, *ApJ*, 808, 107,
doi: [10.1088/0004-637X/808/2/107](https://doi.org/10.1088/0004-637X/808/2/107)
- Das, S., Mathur, S., Nicastro, F., & Krongold, Y. 2019, *ApJL*, 882, L23, doi: [10.3847/2041-8213/ab3b09](https://doi.org/10.3847/2041-8213/ab3b09)
- Everett, J. E., Schiller, Q. G., & Zweibel, E. G. 2010, *ApJ*, 711, 13, doi: [10.1088/0004-637X/711/1/13](https://doi.org/10.1088/0004-637X/711/1/13)
- Everett, J. E., Zweibel, E. G., Benjamin, R. A., et al. 2008, *ApJ*, 674, 258, doi: [10.1086/524766](https://doi.org/10.1086/524766)
- Ferrière, K. M. 2001, *Reviews of Modern Physics*, 73, 1031,
doi: [10.1103/RevModPhys.73.1031](https://doi.org/10.1103/RevModPhys.73.1031)
- Field, G. B. 1965, *ApJ*, 142, 531, doi: [10.1086/148317](https://doi.org/10.1086/148317)
- Fujita, Y., Ohira, Y., & Yamazaki, R. 2013, *ApJL*, 775, L20, doi: [10.1088/2041-8205/775/1/L20](https://doi.org/10.1088/2041-8205/775/1/L20)
- Gabici, S., Evoli, C., Gaggero, D., et al. 2019, *International Journal of Modern Physics D*, 28, 1930022,
doi: [10.1142/S0218271819300222](https://doi.org/10.1142/S0218271819300222)
- Girichidis, P., Pfrommer, C., Hanasz, M., & Naab, T. 2020, *MNRAS*, 491, 993, doi: [10.1093/mnras/stz2961](https://doi.org/10.1093/mnras/stz2961)
- Girichidis, P., Pfrommer, C., Pakmor, R., & Springel, V. 2022, *MNRAS*, 510, 3917, doi: [10.1093/mnras/stab3462](https://doi.org/10.1093/mnras/stab3462)
- Girichidis, P., Werhahn, M., Pfrommer, C., Pakmor, R., & Springel, V. 2024, *MNRAS*, 527, 10897,
doi: [10.1093/mnras/stad3628](https://doi.org/10.1093/mnras/stad3628)
- Gupta, A., Mathur, S., Kingsbury, J., Das, S., & Krongold, Y. 2023, *Nature Astronomy*, 7, 799,
doi: [10.1038/s41550-023-01963-5](https://doi.org/10.1038/s41550-023-01963-5)
- Hayakawa, T., & Fukui, Y. 2022, arXiv e-prints,
arXiv:2208.13406, doi: [10.48550/arXiv.2208.13406](https://doi.org/10.48550/arXiv.2208.13406)
- Haywood, M., Lehnert, M. D., Di Matteo, P., et al. 2016, *A&A*, 589, A66, doi: [10.1051/0004-6361/201527567](https://doi.org/10.1051/0004-6361/201527567)
- Inutsuka, S.-i., Inoue, T., Iwasaki, K., & Hosokawa, T. 2015, *A&A*, 580, A49, doi: [10.1051/0004-6361/201425584](https://doi.org/10.1051/0004-6361/201425584)
- Kakiuchi, K., Suzuki, T. K., Inutsuka, S.-i., Inoue, T., & Shimoda, J. 2024, *ApJ*, 966, 230,
doi: [10.3847/1538-4357/ad3638](https://doi.org/10.3847/1538-4357/ad3638)
- Kamae, T., Karlsson, N., Mizuno, T., Abe, T., & Koi, T. 2006, *ApJ*, 647, 692, doi: [10.1086/505189](https://doi.org/10.1086/505189)
- Kamae, T., Karlsson, N., Mizuno, T., Abe, T., & Koi, T. 2007, *The Astrophysical Journal*, 662, 779,
doi: [10.1086/513602](https://doi.org/10.1086/513602)
- Kataoka, J., Sofue, Y., Inoue, Y., et al. 2018, *Galaxies*, 6, 27, doi: [10.3390/galaxies6010027](https://doi.org/10.3390/galaxies6010027)
- Kataoka, J., Tahara, M., Totani, T., et al. 2013, *ApJ*, 779, 57, doi: [10.1088/0004-637X/779/1/57](https://doi.org/10.1088/0004-637X/779/1/57)
- Kelner, S. R., Aharonian, F. A., & Bugayov, V. V. 2006, 034018, 1, doi: [10.1103/PhysRevD.74.034018](https://doi.org/10.1103/PhysRevD.74.034018)
- Koyama, H., & Inutsuka, S.-i. 2002, *ApJL*, 564, L97,
doi: [10.1086/338978](https://doi.org/10.1086/338978)
- Koyama, K. 2018, *PASJ*, 70, R1, doi: [10.1093/pasj/psx084](https://doi.org/10.1093/pasj/psx084)
- Kroupa, P. 2001, *MNRAS*, 322, 231,
doi: [10.1046/j.1365-8711.2001.04022.x](https://doi.org/10.1046/j.1365-8711.2001.04022.x)
- Meliani, Z., Cristofari, P., Rodríguez-González, A., et al. 2024, *A&A*, 683, A178,
doi: [10.1051/0004-6361/202347352](https://doi.org/10.1051/0004-6361/202347352)
- Mertsch, P., & Petrosian, V. 2019, *A&A*, 622, A203,
doi: [10.1051/0004-6361/201833999](https://doi.org/10.1051/0004-6361/201833999)
- Mertsch, P., & Sarkar, S. 2011, *PhRvL*, 107, 091101,
doi: [10.1103/PhysRevLett.107.091101](https://doi.org/10.1103/PhysRevLett.107.091101)
- Misiriotis, A., Xilouris, E. M., Papamastorakis, J., Boumis, P., & Goudis, C. D. 2006, *A&A*, 459, 113,
doi: [10.1051/0004-6361:20054618](https://doi.org/10.1051/0004-6361:20054618)
- Miyamoto, M., & Nagai, R. 1975, *PASJ*, 27, 533
- Mori, K., Tsuru, T. G., Nakazawa, K., et al. 2022, in *Society of Photo-Optical Instrumentation Engineers (SPIE) Conference Series*, Vol. 12181, Society of Photo-Optical Instrumentation Engineers (SPIE) Conference Series, ed. J.-W. A. den Herder, S. Nikzad, & K. Nakazawa, 1218122, doi: [10.1117/12.2628772](https://doi.org/10.1117/12.2628772)
- Nakashima, S., Inoue, Y., Yamasaki, N., et al. 2018, *ApJ*, 862, 34, doi: [10.3847/1538-4357/aacceeb](https://doi.org/10.3847/1538-4357/aacceeb)
- Navarro, J. F., Frenk, C. S., & White, S. D. M. 1996, *ApJ*, 462, 563, doi: [10.1086/177173](https://doi.org/10.1086/177173)
- Nguyen, D. D., & Thompson, T. A. 2022, *ApJL*, 935, L24,
doi: [10.3847/2041-8213/ac86c3](https://doi.org/10.3847/2041-8213/ac86c3)
- Nishiwaki, K., Asano, K., & Murase, K. 2021, *The Astrophysical Journal*, 922, 190,
doi: [10.3847/1538-4357/ac1cdb](https://doi.org/10.3847/1538-4357/ac1cdb)
- Owen, E. R., & Yang, H. Y. K. 2022, *MNRAS*, 516, 1539,
doi: [10.1093/mnras/stac2289](https://doi.org/10.1093/mnras/stac2289)
- Predehl, P., Sunyaev, R. A., Becker, W., et al. 2020, *Nature*, 588, 227, doi: [10.1038/s41586-020-2979-0](https://doi.org/10.1038/s41586-020-2979-0)
- Sarkar, K. C. 2024, *A&A Rv*, 32, 1,
doi: [10.1007/s00159-024-00152-1](https://doi.org/10.1007/s00159-024-00152-1)
- Sarkar, K. C., Mondal, S., Sharma, P., & Piran, T. 2023, *ApJ*, 951, 36, doi: [10.3847/1538-4357/acd75d](https://doi.org/10.3847/1538-4357/acd75d)
- Sasaki, K., Asano, K., & Terasawa, T. 2015, *ApJ*, 814, 93,
doi: [10.1088/0004-637X/814/2/93](https://doi.org/10.1088/0004-637X/814/2/93)

- Schlickeiser, R. 1989, *ApJ*, 336, 243, doi: [10.1086/167009](https://doi.org/10.1086/167009)
- . 2002, *Cosmic Ray Astrophysics*
- Shapiro, P. R., & Field, G. B. 1976, *ApJ*, 205, 762, doi: [10.1086/154332](https://doi.org/10.1086/154332)
- Shimoda, J., & Inutsuka, S.-i. 2022, *ApJ*
- Shimoda, J., Inutsuka, S.-i., & Nagashima, M. 2024, *PASJ*, 76, 81, doi: [10.1093/pasj/psad081](https://doi.org/10.1093/pasj/psad081)
- Strong, A. W., Moskalenko, I. V., Reimer, O., Digel, S., & Diehl, R. 2004, *A&A*, 422, L47, doi: [10.1051/0004-6361:20040172](https://doi.org/10.1051/0004-6361:20040172)
- Su, M., & Finkbeiner, D. P. 2012, *ApJ*, 753, 61, doi: [10.1088/0004-637X/753/1/61](https://doi.org/10.1088/0004-637X/753/1/61)
- Su, M., Slatyer, T. R., & Finkbeiner, D. P. 2010, *ApJ*, 724, 1044, doi: [10.1088/0004-637X/724/2/1044](https://doi.org/10.1088/0004-637X/724/2/1044)
- Sukhbold, T., Woosley, S. E., & Heger, A. 2018, *ApJ*, 860, 93, doi: [10.3847/1538-4357/aac2da](https://doi.org/10.3847/1538-4357/aac2da)
- Tan, B., & Fielding, D. B. 2024, *MNRAS*, 527, 9683, doi: [10.1093/mnras/stad3793](https://doi.org/10.1093/mnras/stad3793)
- Tan, B., Oh, S. P., & Gronke, M. 2023, *MNRAS*, 520, 2571, doi: [10.1093/mnras/stad236](https://doi.org/10.1093/mnras/stad236)
- Tashiro, M., Maejima, H., Toda, K., et al. 2020, in *Society of Photo-Optical Instrumentation Engineers (SPIE) Conference Series*, Vol. 11444, Society of Photo-Optical Instrumentation Engineers (SPIE) Conference Series, 1144422, doi: [10.1117/12.2565812](https://doi.org/10.1117/12.2565812)
- Teraki, Y., & Asano, K. 2019, *ApJ*, 877, 71, doi: [10.3847/1538-4357/ab1b13](https://doi.org/10.3847/1538-4357/ab1b13)
- Thomas, T., Pfrommer, C., & Pakmor, R. 2023, *MNRAS*, 521, 3023, doi: [10.1093/mnras/stad472](https://doi.org/10.1093/mnras/stad472)
- Tumlinson, J., Peebles, M. S., & Werk, J. K. 2017, *ARA&A*, 55, 389, doi: [10.1146/annurev-astro-091916-055240](https://doi.org/10.1146/annurev-astro-091916-055240)
- Wakker, B. P., & van Woerden, H. 1997, *ARA&A*, 35, 217, doi: [10.1146/annurev.astro.35.1.217](https://doi.org/10.1146/annurev.astro.35.1.217)
- Yamamoto, M., Kataoka, J., & Sofue, Y. 2022, *MNRAS*, 512, 2034, doi: [10.1093/mnras/stac577](https://doi.org/10.1093/mnras/stac577)
- Yang, H. Y. K., & Ruszkowski, M. 2017, *ApJ*, 850, 2, doi: [10.3847/1538-4357/aa9434](https://doi.org/10.3847/1538-4357/aa9434)
- Yang, H. Y. K., Ruszkowski, M., & Zweibel, E. G. 2022, *Nature Astronomy*, 6, 584, doi: [10.1038/s41550-022-01618-x](https://doi.org/10.1038/s41550-022-01618-x)